

Atomic tunnel arrays

B.P. ANDERSON and M.A. KASEVICH

Physics Department, Yale University, New Haven, CT 06520-8120, USA

1. – Introduction

The demonstration of Bose-Einstein condensation in atomic gases [1] raises the possibility of exploring relationships between coherence properties of atom vapor condensates [2, 3, 4, 5], superfluid He [6, 7], and superconductivity [8]. These quantum systems share common theoretical framework and exhibit similar observable characteristics. In this lecture, we discuss observed behavior [9] of an optically trapped Bose-Einstein condensate (BEC) analogous to the Josephson effect of superconducting systems.

2. – Josephson effects in superconductors

Josephson effects are a range of phenomena exhibited by two superconductors separated by a thin insulating barrier. Cooper pair electron tunneling through the barrier couples the dynamics of the two macroscopically occupied quantum states. Under appropriate conditions [10, 11], the wavefunction of each superconductor can be approximated as

$$(1) \quad \Psi_q = n_q^{1/2} e^{i\phi_q(t)},$$

where q represents either superconductor 1 or 2, n is the Cooper pair number density of the ground state system, and ϕ is the relative macroscopic phase. In the absence of coupling, the number density of each superconductor remains constant with time, and the phase evolves at a rate of μ/\hbar , where μ is the chemical potential.

For weakly coupled superconductors, the equations of motion are written

$$(2) \quad i\hbar \frac{\partial \Psi_1}{\partial t} = \mu_1 \Psi_1 + K \Psi_2,$$

$$(3) \quad i\hbar \frac{\partial \Psi_2}{\partial t} = \mu_2 \Psi_2 + K \Psi_1,$$

where K represents the strength of the coupling due to tunneling. By inserting eq. 1 for Ψ_1 and Ψ_2 into eqs. 2 and 3, one obtains

$$(4) \quad \frac{\partial n_1}{\partial t} = 2(K/\hbar)n_1^{1/2}n_2^{1/2} \sin(\phi_2 - \phi_1),$$

$$(5) \quad \frac{\partial n_2}{\partial t} = -\frac{\partial n_1}{\partial t},$$

$$(6) \quad \frac{\partial(\phi_2 - \phi_1)}{\partial t} = -(\mu_2 - \mu_1)/\hbar.$$

The first two of these equations describe the rate of change of electron densities, while the third describes the evolution of the phase difference between the two wavefunctions, valid for large n_1 and n_2 , with $n_1 \simeq n_2$.

When a dc voltage V is applied across the tunnel junction, the chemical potential difference is given by $\mu_2 - \mu_1 = 2eV$, resulting in linear evolution of the phase difference (phase slip). The flux of particles through the barrier can be written as an oscillating current:

$$(7) \quad I = I_0 \sin(\phi_2(t) - \phi_1(t)) = I_0 \sin(2eVt/\hbar + \Delta\phi(0)),$$

where the amplitude I_0 is proportional to the strength of the coupling, and $\Delta\phi(0)$ is the initial relative phase difference. This ac current modulation, arising from the application of a dc voltage, is the ac Josephson effect. The modulation frequency, $\omega_J = 2eV/\hbar$, is determined only by the chemical potential difference. This voltage-frequency relation has enabled the Josephson effect to contribute to the determination of $2e/\hbar$ and the volt [12]. High accuracy is achieved through the conversion of voltages into frequency measurements.

3. – General approach

Our experiment involved the creation of a ^{87}Rb BEC in a time-averaged orbiting potential (TOP) trap [13] and the subsequent transfer of the BEC to a one-dimensional periodic potential formed by a vertically oriented standing wave of far-detuned laser light [14]. To create the standing wave, we used a retro-reflected laser beam, hence the potential had a periodicity of half of the laser wavelength λ .

The depths of the potential wells were determined by the intensity in the laser beam. We loaded a subset of the potential wells with atoms from the BEC, forming an array of atom traps with initially identical relative macroscopic phases. Because the standing

wave had a vertical orientation, the gravitational potential energy difference between adjacent potential wells created a difference in chemical potentials. In our experiments, the depths of the wells had maximum values of $\sim 2.1E_R$, where $E_R = \hbar^2 k^2 / 2m$ is the photon recoil energy, with $k = 2\pi/\lambda$. For potential depths of this magnitude, only one bound state existed in each potential well.

Our configuration was similar to a superconducting Josephson junction. The main differences were that we used macroscopic quantum states composed of neutral atoms instead of Cooper pairs of electrons, and that we had an array of such states separated by potential barriers, instead of just two states. The goal of our experiment was to observe a periodic atom current due to the temporal interference of the macroscopically filled states in the trap array.

4. – Atomic tunnel array: theory

As was the case for superconductors, we begin our theoretical analysis by writing the macroscopic wavefunction for a BEC as $\Psi = n^{1/2} e^{i\phi(t)}$. In this case, n is the number density of atoms in the condensate. With a vertically oriented array of such quantum states, the wavefunction that describes the q^{th} lattice state is given by $\Psi_q = n_q^{1/2} e^{i\phi_q(t)}$. Again, n_q is determined by the single particle wavefunction and the number of atoms in the q^{th} lattice state. Now, however, the macroscopic phase $\phi_q(t)$ depends upon the initial relative phase at time $t = 0$ and the gravitational potential energy at the q^{th} lattice site.

4.1. Model system. – The array of atom traps can be modeled as an array of point-source emitters of de Broglie waves when tunneling is considered. The traps at positions z_q^0 emit waves which then travel in a continuum, accelerating with the pull of gravity (the effect of the lattice is neglected after tunneling) out of trapped states. The rate of emission is proportional to the tunneling probability of atoms out of the lattice array potential wells, and depends upon the potential depths of the traps. The energy $\hbar\omega_q$ of each wave depends upon the lattice site from which it was emitted, with a chemical potential difference of $\hbar\omega_J = mg\lambda/2$ between adjacent wells (m is the mass of an atom). The momentum gained by each wave depends upon the distance over which it has traveled, and is given by $\hbar k_q = m\sqrt{2g|z - z_q^0|}$, where z is the spatial coordinate. The relative phase of each wave depends upon the initial phase ϕ_q^0 of the emitter at time $t = 0$.

The wavefunction of the total array output can then be written as a sum of the output of N emitters:

$$(8) \quad \Psi(z, t) = \sum_{q=1}^N A_q(t) \exp[i \int (k_q dz - \omega_q dt + \phi_q^0)].$$

Here, $A_q(t)$ parameterizes both the initial wavefunction amplitude (number of atoms) and depletion of the q^{th} lattice state due to tunneling. Because the frequencies ω_q are equally spaced by an increment ω_J , the probability of atom detection at a point below the array will be periodic with that frequency. In other words, this model predicts the

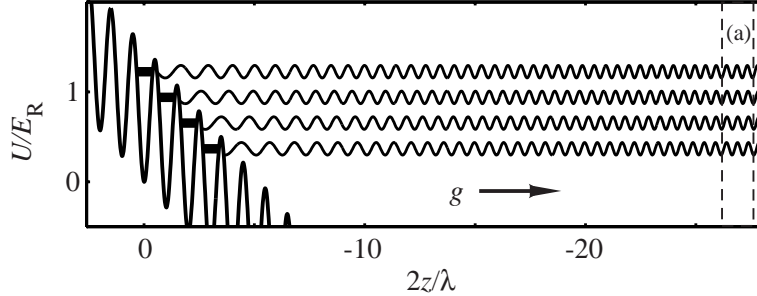


Fig. 1. – The effective optical plus gravitational potential U/E_R for our experimental parameters, where E_R is the photon recoil energy. Bound states of the potential are represented by heavy lines. The de Broglie wave output, which constructively interferes in region (a), is represented by horizontal waves.

periodic detection of groups of atoms due to periodic constructive interference of the emitted de Broglie waves. Figure 1 depicts a sloping periodic potential with de Broglie wave emission from a set of the emitters in the lattice array. At points where the waves are in phase, a pulse is formed.

In this respect, the output of the atomic tunnel array is analogous to the output of a mode-locked laser [15], in which a set of frequencies spaced at regular frequency intervals is generated within a laser cavity. The emitted frequency modes have a definite linear phase relationship. At points where the emitted waves are in phase, constructive interference causes the formation of a pulse of light, similar to the model presented above for the atomic tunnel array. However, if a random phase relationship exists between the modes, pulses will not form. Rather, a semi-continuous output is obtained due to the inability of the modes to constructively interfere. Similarly, in the atomic tunnel array model, random initial phases for ϕ_q^0 prohibit the formation of periodic atom pulses at the expected frequency.

Sample computed output from the tunnel array model is shown in fig. 2(a), calculated for a set of 30 traps, or emitters. Although depletion of the traps is neglected in the calculation, the initial amplitudes of the wells are given a Gaussian envelope distribution. The amplitude of each pulse increases with time as the spatial pulse width narrows. The widths of the pulses depend upon the number of wells used in the calculation — increasing numbers of lattice sites produce increasingly more narrow pulses. If random initial phases are used in the calculation, pulses no longer form, as shown in fig. 2(b).

4.2. Quantum calculation. – A full quantum mechanical calculation to determine the tunnel array behavior would involve the effects of interactions between atoms. However, in a periodic potential of the geometry described above, and for low enough atomic densities, mean-field interaction energies are much smaller than the bound state energies of atoms in the potential wells. To a good approximation, the behavior of the atomic tunnel array can then be calculated with the time-dependent Schrödinger equation (TDSE), ne-

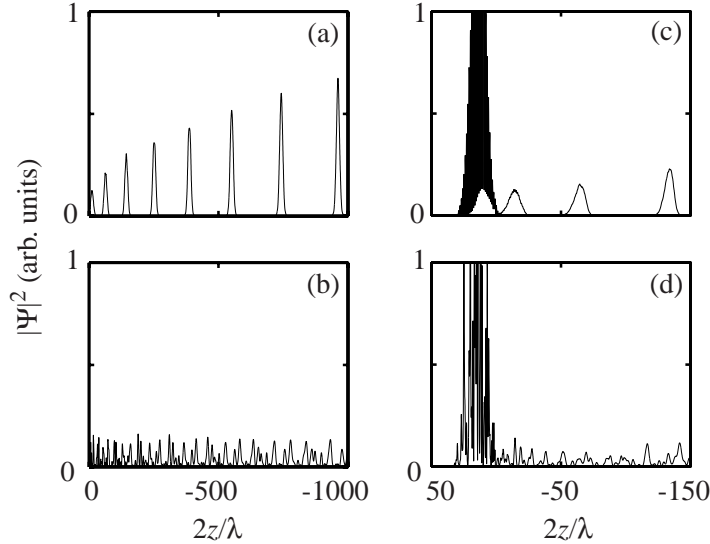


Fig. 2. – (a) Output from the tunnel array model (eq. 7), evaluated at 10 ms. Initial phases are identical. The tunnel array source, not shown in the plot, is located immediately to the left of the $z = 0$ point. (b) Model output for random initial phases. (c) Numerical solution to the Schrödinger equation showing the confined wavefunction and three output pulses, evaluated at 3.8 ms. (d) Numerical solution for random initial phases.

glecting mean-field effects. We solve the TDSE using standard numerical methods [16]. We take the initial wavefunction to be the sum of individual wavefunctions, each with a Gaussian density distribution and a specified initial relative phase. The individual wavefunctions are initially centered at the lattice sites. The width of each state is determined by the ground state energy of a harmonic oscillator which best approximates the shape of an individual potential well in the array. The depths of the wells are $\sim 1.4E_R$. At this potential depth, only a single bound state exists in each well, as depicted by the heavy lines in fig. 1.

The total probability distribution from a sample calculation is shown in fig. 2(c) for 30 populated wells. The initial phases of the lattice states are identical, and the initial amplitudes correspond to a Gaussian envelope distribution. Three pulses are shown falling from the oscillating source. Figure 2(d) shows the result of a similar calculation with random initial phases. The calculations confirm the validity of the tunnel array model, displaying the same behavior that the model predicts. With these calculations, we verified the accuracy of the assumption that the lattice has a negligible effect on the pulses in the continuum.

The calculations also graphically show a link between the Bloch oscillations [17, 18] of the confined wavefunctions and the formation of pulses, shown in detail in fig. 3. Upon numerically solving the Schrödinger equation, the center of mass of the total wavefunction

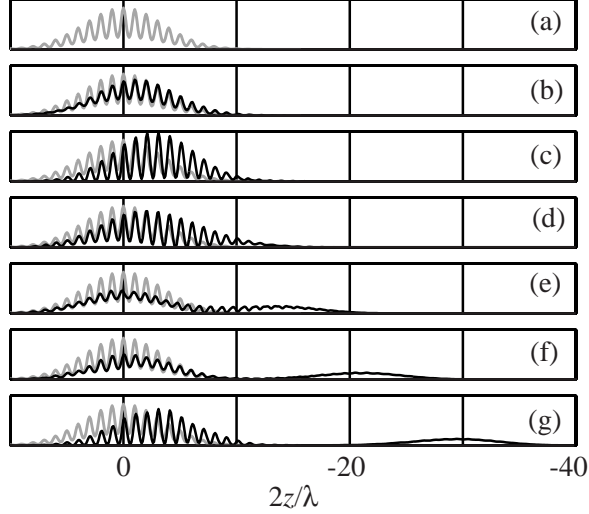


Fig. 3. – Time development of the wavefunction in the periodic potential. (a) The initial wavefunction is shown in gray. The oscillating wavefunction, in black, is shown at times (b) $T_J/4$, (c) $T_J/2$, (d) $3T_J/4$, (e) T_J , (f) $5T_J/4$, and (g) $3T_J/2$. T_J is the Josephson oscillation period, $T_J = 2\pi/\omega_J$. For reference, the position of the initial wavefunction is shown in gray in all plots. The plots show the oscillations and depletion of the total wavefunction and pulse formation.

is observed to undergo longitudinal spatial oscillations with a frequency of ω_J . At the turning point of each oscillation, a fraction of the wavefunction continues to propagate in the direction of gravity, forming a pulse.

4.3. Interband tunneling. – The formation of pulses can be viewed as interband tunneling at the turning point of a Bloch oscillation, as described by Zener for dielectric breakdown in metals [18]. Zener considered a multiple energy band lattice with a linear potential gradient created by an external field. The field induces oscillations of the confined energy states of the periodic potential, and the highest probability of tunneling to the next higher lying energy band occurs at the diffraction point of a Bloch cycle. In our case, atoms confined to the lowest energy band (the trapped atoms) will oscillate at the Bloch frequency $mg\lambda/2\hbar$, identical to the Josephson frequency ω_J . The gravitational field induces tunneling into the next higher lying state (the unbound continuum). Analogous to the calculations of Zener, the tunneling probability per oscillation for our lattice is given by

$$(9) \quad P = \exp\left(-\frac{\lambda\epsilon^2}{8\hbar^2g}\right),$$

where ϵ is the energy gap between the ground state energy band and the continuum states. Not only is this picture consistent with the solution of the Schrödinger equation as described above, but it suggests that atom pulses are a direct indication of an oscillating atom current flowing between the lattice sites, and thus that pulses are a signature of a type of Josephson effect.

For the parameters used in our experiment, the assumption that atoms are confined to single wells is not entirely accurate. In a periodic potential without an external force, the energy eigenstates of the system are the Bloch states. When a potential gradient is applied, the Bloch states undergo coherent oscillations, with wavepackets remaining confined to a single energy band. Such oscillations have been previously observed for non-degenerate atoms trapped in an optical standing wave [19]. The Wannier-Stark states ψ_p [20, 21] form an alternative but equivalent basis to the Bloch states. Each state is a superposition of localized Wannier (tight-binding) states w_q : $\psi_p = \sum_q J_{q-p}(4T/mg\lambda)w_q$, where J_n is the n^{th} order Bessel function and T is the tunneling matrix element between lattice sites. For our parameters, each lattice state has a spatial extent that covers a small cluster of potential wells, with most of the atoms of each state concentrated at the central lattice site. Pulsed atom output is still expected; however, for simplicity in our calculations and in the physical descriptions, states were assumed to localize to single lattice sites.

5. – Trapping a BEC in an optical lattice

After loading $\sim 10^8$ atoms into a magneto-optic trap [22], the trapped atoms were optically pumped into the $F = 2, m_f = 2$ Rb ground state, loaded into a TOP trap, and evaporatively cooled to create a condensate using ramping radio-frequency and confining magnetic fields [23]. We typically created nearly pure condensates of $\sim 10^4$ atoms with radial sizes of $\sim 8\mu\text{m}$ [24].

To create the 1-D optical potential, we retro-reflected a vertically oriented $\lambda = 850$ nm laser beam. The beam created a series of potential wells centered at the anti-nodes of the standing wave with a spacing of $\lambda/2$. The beam was focused to a $1/e^2$ beam waist of $\sim 80\mu\text{m}$ (radius), with maximum intensities of ~ 80 W/cm². The maximum depths of the wells were $\sim 2.1E_R$, only enough to support a single bound state. The large detuning of the beam (70 nm red-detuned from the 780 nm Rb transitions) gave a photon scattering rate of less than 0.01 s⁻¹.

To load the condensed atoms into the potential wells, the spring constants of the magnetic trap first had to be relaxed. The control of density and size of the BEC allowed for adjustment of the number of wells loaded and the densities (and hence mean-field interactions) of the atoms in the wells. After the adiabatic relaxation, the standing wave potential was ramped on (using an acousto-optic modulator) in ~ 20 ms. At this point, the standing wave overlapped the magnetically trapped BEC. The dc component of the TOP trap was then turned off, while the rotating component remained on to maintain the spin polarization of the atoms, completing the transfer of atoms into the optical

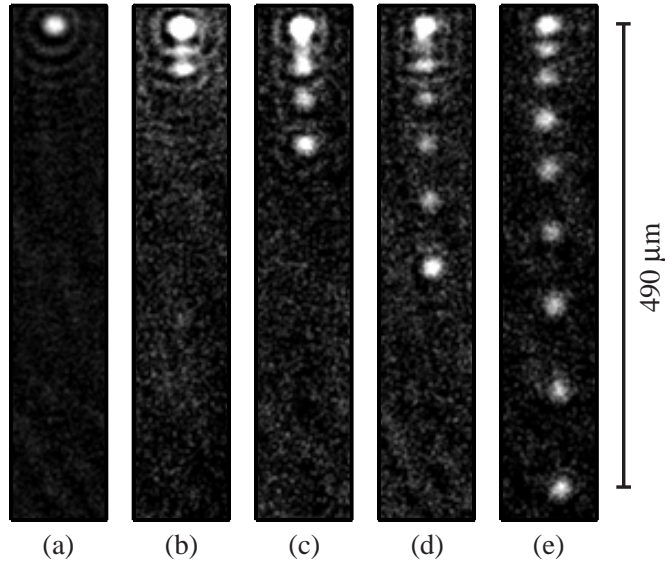


Fig. 4. – (a) Absorption image of a BEC in a weak TOP trap. (b)-(e): Absorption images taken after transferring the atoms into the optical lattice and allowing (b) 3 ms, (c) 5 ms, (d) 7 ms, and (e) 10 ms of tunneling.

lattice.

6. – Atomic tunnel array: observations

In this section, we describe observations of the dynamics of the atomic tunnel arrays. The distributions of atoms were observed with absorption imaging. For observations that were made as a function of time, a new BEC and tunnel array were created for each time step due to the destructive process of absorption imaging. In the following descriptions, a high intensity lattice refers to trap depths of $\sim 2.1E_R$, and a low intensity lattice refers to trap depths of $\sim 1.4E_R$. We typically loaded about 30 potential wells, with up to ~ 1000 atoms per potential well.

6.1. Low Intensity lattice. – When we turned on the optical trap at a low intensity, we observed pulses of atoms falling from the trap, as shown in fig. 4 for various time delays. Images (b)-(e), with identical intensity scales, show saturated images of the lattice array in order to highlight the pulses. For comparison, fig. 4(a) shows an unsaturated image of a magnetically trapped BEC. Due to limits in optical resolution, individual lattice sites are not resolvable. In each of images (b)-(e), the pulse at the lowest part of the image was the first emitted pulse. The last emitted pulse was not resolvable from the image of the trap array.

The measurement of fig. 4(e) was made 10 ms after the atoms were loaded into the

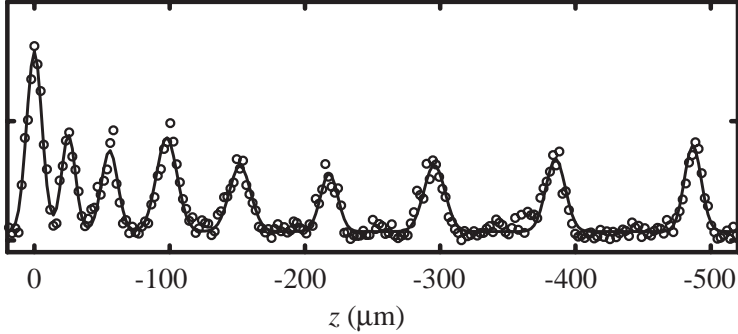


Fig. 5. – The integrated absorption cross section for fig. 4(e), obtained by summing over the horizontal profile. The circles are the data. The solid line is a non-linear least squares fit to a series of Gaussian pulses, constrained to be separated by a fixed time interval, with g as a fitting parameter.

optical trap. Each pulse contained ~ 1000 atoms. The output of the tunnel array was similar to the output expected based on our model and calculations. We measured the spatial separations of the pulses in the images, and with a value of 9.8 m/s^2 for g , we inferred the time intervals between the pulses. The measured period of $1.10 \pm 0.05 \text{ ms}$ agreed well with the expected value of $T_J = 2\pi/\omega_J = 1.09 \text{ ms}$. The uncertainty in the measurement was limited by the uncertainty in the calibration of the imaging system. Pulses were also observed for less intense optical traps of $\sim 1E_R$. In these cases, the tunnel array was depleted more quickly, with more atoms per pulse but fewer pulses (up to four). The pulse frequency however remained the same. Because well defined bound states should not exist at this trap depth, the pulses could be interpreted as the result of above-barrier quantum reflections.

We integrated over the transverse absorption profile of fig. 4(e) to produce the cross section shown in fig. 5. We fit the cross section with a series of Gaussian distributions constrained to be periodic in time, resulting in a measurement of $9.6 \pm 0.4 \text{ m/s}^2$ for g , with the error again dominated by imaging calibration uncertainty. The measurement resolution was $\delta g \sim 10^{-4}g$, or $\delta g \sim 10^{-5}g/\sqrt{Hz}$ for the 10 ms measurement. The accuracy of the measurement might be improved by using a resonant probe laser beam and fluorescence detector to determine the temporal distribution of the atom pulses, thereby eliminating uncertainties due to the imaging system. The resolution of the measurement may also be enhanced by generating pulses at higher frequencies. This could be accomplished by increasing the trapping laser wavelength, using a different laser beam geometry, or by combining standing waves of different frequencies to form a super-lattice.

6.2. High intensity lattice. – When we loaded the atoms into the high intensity lattice, we measured trap lifetimes of $\sim 50 \text{ ms}$, much shorter than would be expected due to 3-

body recombination [25] or to off-resonant photon scattering. However, the lifetime is consistent with tunneling time estimates based on our numerical calculations and the tunneling probability formula of eq. 9 for $\epsilon \sim E_R$. Pulses of atoms were not observed in this case, possibly due to a relatively low number of atoms per pulse.

6.3. Hold and Release. – In this experiment, the BEC was loaded into a high intensity lattice and held for a variable time (~ 5 ms) before the lattice was suddenly turned off. The atom distribution was measured after a subsequent 5 ms of ballistic expansion. Because of the Fourier relationship between the spatial and momentum distributions of a ground state wavefunction, the ballistic expansion images provided a measurement of the momentum distribution of the trapped atoms as well as information about the initial spatial confinement of the atoms. To model the ballistically expanding atom wavepackets, we assumed an initial set of traps with the distribution of atoms localized to $\sim \lambda/4$ within each well (minimal coupling). The number of atoms in each well was determined by the position of the well in a Gaussian envelope distribution encompassing all of the wells. The Fourier transform of this spatial distribution is a set of wavepackets distributed over momentum-space. The $2\hbar k$ spacing between the momentum-space wavepackets is determined by the $\lambda/2$ spatial separation between the traps. The widths of the wavepackets are identical, and are determined by the number of traps in the spatial distribution.

The number of momentum-space wavepackets that can be observed is determined by the initial spatial localization of the individual traps. For our experimental parameters (trap localization of $\sim \lambda/2$), this corresponds to only one or two visible peaks in the momentum distribution. Tighter confinement within each well, with the same periodicity, would produce more visible momentum peaks (via the Heisenberg uncertainty relations). Weaker confinement would produce a single momentum peak, but the width of the peak would broaden. The precise momentum distribution depends on the relative phase between adjacent traps. Figure 6 shows the expected velocity distributions for atoms released from an optical trap with ~ 30 wells loaded, with spatial localization of $\lambda/4$, for three relative phase differences. Figure 7 shows the velocity distributions for various confinements and numbers of wells loaded, with π rad phase shifts between adjacent wells.

Experimentally, when we let the trapped atoms ballistically expand after a fixed holding time in a high intensity lattice, we observed a single prominent momentum peak and a single minor peak after 5 ms of expansion. The distribution of atoms among momentum components varied with the relative phases of the atoms as they were released from the traps. The relative phases evolved with time due to the differences in gravitational potential energy. The separation between peaks was $\sim 54 \pm 4 \mu\text{m}$, agreeing well with the expected separation of $2v_R \cdot (5 \text{ ms}) = 54 \mu\text{m}$. This process was a signature of the time-domain interference of the macroscopic states of the source. Figure 8 shows the observed time of flight pattern for three hold times.

6.4. Dephasing and loss of coherence. – We expected the phase coherence of the lattice array states to be lost due to the mean-field interaction of the atoms. At potential well

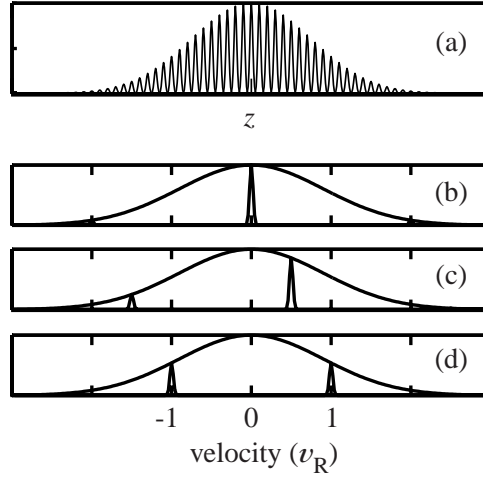


Fig. 6. – (a) The simulated spatial distribution of atoms in the optical trap before release. The plot shows a spatial localization of $\lambda/4$ for the traps, which are separated by $\lambda/2$. The lower plots show the velocity distribution for relative phase differences between wells of (b) 0 rad, (c) $\pi/2$ rad, (d) and π rad. The broad Gaussian distribution in these plots is a relative momentum peak envelope distribution, which grows in width with tighter initial spatial confinement, revealing more velocity peaks separated by $2v_R$ ($v_R = \hbar k/m$).

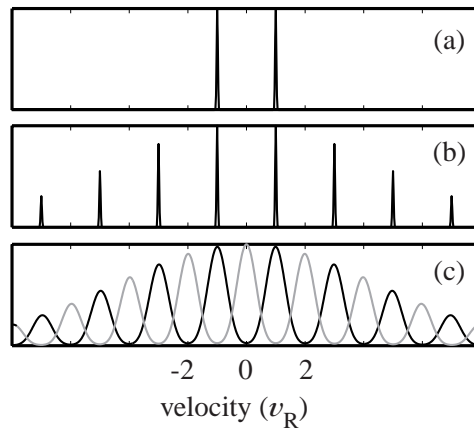


Fig. 7. – The calculated velocity distribution for traps with (a) $\lambda/2$ spatial localization of the wells, and 30 wells loaded, (b) $\lambda/20$ localization and 30 wells loaded, and (c) $\lambda/20$ localization and 2 wells loaded with π rad phase shifts between wells (dark lines) and 0 rad shifts (gray line). This last case is similar to the case of usual 2 slit diffraction.

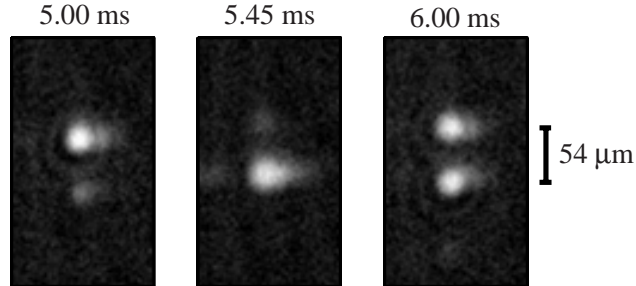


Fig. 8. – Time of flight absorption images, after 5 ms of ballistic expansion. The atoms were held in a high intensity lattice for the times shown, then released.

depths of $1.4E_R$, we calculated a mean-field energy of $\sim 4k_B \cdot \text{nK}$ for our peak densities ($\sim 10^{13} \text{ cm}^{-3}$), much less than the kinetic energy ($\sim E_R = 157k_B \cdot \text{nK}$) of atoms in the traps. Nevertheless, the mean-field interaction will shift the chemical potentials of the trapped atoms by an amount that depends upon the density of atoms in each well. For our parameters, this corresponds to a maximum frequency shift of 80 Hz for the ground state energies. The maximum *relative* frequency shift is 4 Hz between adjacent wells. The result of a frequency shift is a dephasing of the array output due to slight variations in the oscillation frequencies of the tunneling currents. The timescale over which this dephasing happens should be proportional to the density of the traps. For our densities in the low intensity traps, we did not expect to see signs of dephasing in the 10 ms measurements described above. For higher densities and longer measurement times, we expected dephasing to occur.

We observed dephasing of the tunnel array output by first holding the atoms in a high intensity trap for a variable amount of time, then by decreasing the potential depths to $1.4E_R$ in order to induce tunneling. We then imaged the atoms after 5 ms of tunneling in the low intensity traps. The images in fig. 9 show a comparison of pulsed output and dephased output showing a loss of coherence, observed after various holding times in a strong lattice. The dephased output was qualitatively similar to the model output for random initial phases of the lattice states.

7. – Conclusions

The atomic tunnel array can be considered a source of coherent matter-wave or “atom laser” [3] output. As we have discussed, atom pulses from an array can be modeled similarly to pulses of a mode-locked laser. In this respect, the pulsed output that we have observed is a demonstration of a “mode-locked atom laser.” The initial mode-locking is manifested by loading the entire array of traps from a single BEC, ensuring a definite phase relationship between the array states. Estimates of the phase-space densities of the pulses that we observed, based on number of atoms per pulse and pulse velocity

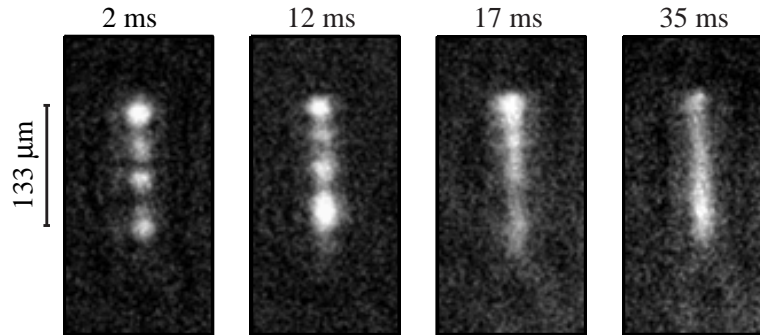


Fig. 9. – Tunnel array output, imaged after 5 ms of tunneling, showing the loss of phase coherence of the trapped atoms. Before inducing tunneling by dropping the intensity of the lattice, the atoms were held at high intensity for the times shown.

spread, indicate that the pulses are in the quantum degenerate regime. Additionally, the observation of periodic pulses is an indication of the coherence length of the array output. We conclude that the coherence length of the output is $> 500\mu\text{m}$, much larger than the dimensions of the resonator (the array).

To conclude, we observed periodic pulsed atom output from atoms trapped in an optical lattice. The pulsed output from our atomic tunnel array can be described using the principles of the Josephson effect, and are additionally a demonstration of a mode-locked atom laser. The subject of Bose-Einstein condensates trapped in optical lattices is rich with possible experiments. The observation of pulses in this experiment is yet another link between the physics of superfluids and superconductors and Bose-Einstein condensation in a dilute atomic gas.

REFERENCES

- [1] Anderson M., Ensher J., Matthews M., Wieman C., Cornell E., *Science*, **269** (1995) 198; Davis K., Mewes M.-O., Andrews M., van Druten N., Durfee D., Kurn D., Ketterle W., *Phys. Rev. Lett.*, **75** (1995) 3969; Bradley C., Sackett C., Tollett J., Hulet R., *Phys. Rev. Lett.*, **75** (1995) 1687; see also, Bradley C., Sackett C., Hulet R., *Phys. Rev. Lett.*, **78** (1997) 985.
- [2] Andrews M., Townsend C., Miesner H.-J., Durfee D., Kurn D., Ketterle W., *Science*, **275** (1997) 637;
- [3] Mewes M.-O., Andrews M., Kurn D., Durfee D., Townsend C., Ketterle W., *Phys. Rev. Lett.*, **78** (1997) 582.
- [4] Burt E., Ghrist R., Myatt C., Holland M., Cornell E., Weiman C., *Phys. Rev. Lett.*, **79** (1997) 337.
- [5] Zapata I., Sols F., Leggett A., *Phys. Rev. A*, **57** (1998) R28.
- [6] Anderson P.W., in *Quantum Fluids (Sussex University Symposium 1965)*, edited by D.F. Brewer (John Wiley and Sons Inc., New York) 1966, pp. 146-173.

- [7] For recent work with superfluid ^3He , see, Pereverzev S., Loshak A., Backhaus S., Davis J., Packard R., *Nature*, **388** (1997) 449; Backhaus S., Pereverzev S., Loshak A., Davis J., Packard R., *Science*, **278** (1997) 1435.
- [8] Josephson B.D., *Phys. Lett.*, **1** (1962) 251; see also, Anderson P.W., in *Lectures on the Many-Body Problem (International Spring School of Physics, 5th 1963)*, edited by E.R. Caianiello (Academic Press, New York) 1964, pp. 113-135; Anderson P., *Basic Notions of Condensed Matter Physics* (Benjamin/Cummings Publishing Co., Menlo Park, CA) 1984, and references therein.
- [9] Anderson B. and Kasevich M., to appear in *Science*.
- [10] See, for example, Barone A. and Paternó G., *Physics and Applications of the Josephson Effect* (John Wiley and Sons, New York) 1982.
- [11] See, for example, Feynman R., *Lectures on Physics*, Vol. 3, (Addison-Wesley, New York) 1965, ch. 21.
- [12] See, for example, Taylor B., Parker W., Langenberg D., *Rev. Mod. Phys.*, **41** (1969) 375.
- [13] Petrich W., Anderson M., Ensher J., Cornell E., *Phys. Rev. Lett.*, **74** (1995) 3352.
- [14] Anderson B., Gustavson T., Kasevich M., *Phys. Rev. A*, **53** (1996) R3727. See also, Friebe S., D'Andrea C., Walz J., Weitz M., Hänsch T., *Phys. Rev. A*, **57** (1998) R20; Müller-Seydlitz T., Hartl M., Brezger B., Hänsel H., Keller C., Schnetz A., Spreeuw R., Pfau T., Mlynek J., *Phys. Rev. Lett.*, **78** (1997) 1038.
- [15] Siegman A., *Lasers*, (University Science Books, Mill Valley, CA) 1986.
- [16] Press W., Flannery B., Teukolsky S., Vetterling W., *Numerical Recipes in C* (Cambridge University Press, Cambridge) 1988, ch. 17.
- [17] Bloch F., *Z. Phys.*, **52** (1928) 555.
- [18] Zener C., *Proc. R. Soc. London A*, **145** (1934) 523.
- [19] Dahan M., Peik E., Reichel J., Castin Y., Salomon C., *Phys. Rev. Lett.*, **76** (1996) 4508.
- [20] Wannier G., *Phys. Rev.*, **117** (1961) 432; Fukuyama H., Bari R., Fogedby H., *Phys. Rev. B*, **8** (1973) 5579; Emin D. and Hart C., *Phys. Rev. B*, **36** (1987) 7353.
- [21] Observation of atomic Wannier-Stark ladders is reported in Wilkinson S., Bharucha C., Madison K., Niu Q., Raizen M., *Phys. Rev. Lett.*, **76** (1996) 4512.
- [22] Raab E., Prentiss M., Cable A., Chu S., Pritchard D., *Phys. Rev. Lett.*, **59** (1987) 2631.
- [23] For a discussion of evaporative cooling, see, Ketterle W. and van Druten N., *Advances in Atomic, Molecular, and Optical Physics*, **37** (1996) 181, and references therein.
- [24] Anderson B. and Kasevich M., to appear in *Phys. Rev. A*.
- [25] From the probe absorption we infer a peak trap density of $\sim 10^{13}$ atoms/cm³. Using the three-body loss coefficient from Fedichev P., Reynolds M., Shlyapnikov G., *Phys. Rev. Lett.*, **77** (1996) 2921, we estimate a collision time of $\sim 4 \times 10^3$ s.